ACS Catalysis

pubs.acs.org/acscatalysis

Research Article

# In−N−In Sites Boosting Interfacial Charge Transfer in Carbon-Coated Hollow Tubular $In_2O_3/ZnIn_2S_4$ Heterostructure Derived from In-MOF for Enhanced Photocatalytic Hydrogen Evolution

Quan Zhang, Juhua Zhang, Xiaohao Wang, Lingfeng Li, Ye-Fei Li, and Wei-Lin Dai*

Cite This: *ACS Catal.* 2021, 11, 6276−6289

Read Online

ACCESS | Metrics & More | Article Recommendations | Supporting Information

**ABSTRACT:** A hierarchical hollow tubular $In_2O_3/ZnIn_2S_4$ heterostructure was rationally designed by growing thin-layered $ZnIn_2S_4$ on the surface of carbon-coated hollow tubular $In_2O_3$ (C/HT-$In_2O_3$) that was derived from In-MOF as a photocatalyst for the photocatalytic hydrogen evolution (PHE) reaction. The fast interfacial charge transfer and significantly enhanced PHE activity could be ascribed to the narrowed band gap of C/HT-$In_2O_3$ and the inclined formation of the staggered heterostructure between C/HT-$In_2O_3$ and $ZnIn_2S_4$. The former was caused by the coordinated In−N−In sites as revealed by EXAFS analysis, while the latter was proved by density functional theory (DFT) calculation. Additionally, the high electronic conduction of carbon for bridging charge separation from C/HT-$In_2O_3$ to $ZnIn_2S_4$ further accelerated the protonation process. It was found that the optimum $H_2$ evolution rate reached 920.5 $\mu$mol/m$^2$ when the mass proportion of counterparts was set at 1:2, about 13.2 and 6.6 times higher than that of pristine C/HT-$In_2O_3$ and $ZnIn_2S_4$, respectively. This work demonstrated the feasibility of establishing coordinated In−N−In sites in the interface of the carbon-coated HT-$In_2O_3/ZnIn_2S_4$ heterostructure for boosting charge transfer and introduced an ideal light-activated catalyst for PHE reactions from water.

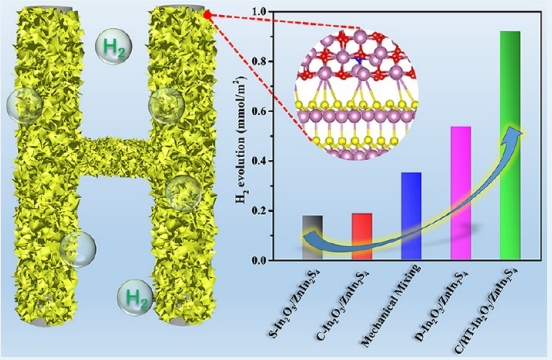


**KEYWORDS:** *In−N−In sites, In-MOF, carbon coated, hollow tubular $In_2O_3/ZnIn_2S_4$, heterostructure, interfacial charge transfer, photocatalytic hydrogen evolution*

## 1. INTRODUCTION

To survive and develop in the background of limited fossil energy reserves is currently an important topic, as fossil fuels are irreplaceable for the moment and possibly even longer.[1−3] Thus, the exploration of alternative energy would be highly beneficial to postpone the end of the "fossil energy era" and alleviate an energy crisis in the future.[4−6]

Under the dual requirements of environmental protection and energy utilization, hydrogen has always been a broad public interest in recent years because of its ideal calorific value and zero carbon energy attributes, meaning that it can act as a potentially green and sustainable energy in the long term.[7−9] Focusing on cheaply producing hydrogen in large quantities, studies have always been searching for the high efficiency of catalysts for photocatalytic hydrogen evolution (PHE) to achieve the solar-to-hydrogen conversion. Currently, many exciting investigations toward enhancing PHE reactions have been successively reported, contributing significantly to the design and synthesis of advanced photocatalysts.[10−16] Though the PHE reaction was regarded as a single-electron-reduction process, the prolonged lifetime of photogenerated electrons and the rate of hydrogen production in this field have not yet lived up to expectations because of the inefficiency of catalysts, all demonstrating an insufficient PHE response for solar-to-hydrogen conversion with large-scale quantities. To solve the economic unreliability of PHE reactions, many ingenious strategies have been, therefore, adopted by adjusting the band alignment of semiconductors,[17] regulating ion/metal deposition,[18] fabricating heterojunction structures,[19,20] making atomically dispersed metal sites,[21,22] and so on. Among them, the engineering of a hierarchical heterostructure was considered to be a pioneering strategy to effectively drive the separation of charge carriers.[23−26] However, not all materials were suitable for the fabrication of a heterostructure, and in most cases, the heterostructure required that the energy levels of the matched counterparts should be overlapped partially.[27] Even though not all constructed heterostructures spontaneously promoted the charge separation in PHE reactions because of the induction of

Received: December 16, 2020
Revised: April 27, 2021
Published: May 10, 2021

**Scheme 1. Schematic Illustration of the Synthetic Process of C/HT-$In_2O_3$/$ZnIn_2S_4$**

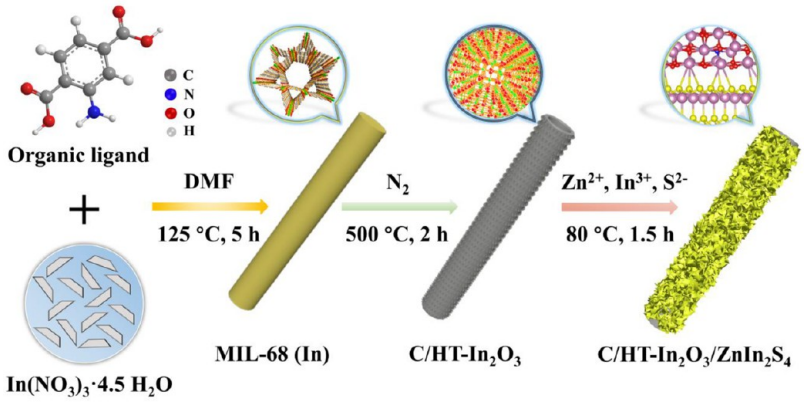


light, the adsorption of water molecules, the dynamic recombination, and separation of electron−hole pairs were complex and mixed together;[28] thus, we were usually uncertain about the specific species and only judged the PHE efficiency by measuring the final hydrogen production rate or amount. The atomic investigation of species at the heterostructure interface was, therefore, of significant importance for clarifying these issues. Additionally, the electronic configuration at an interfacial heterostructure was different from that of a single component, while the precise revelation of atomic collocation and local phase composition to favor the PHE reactions have not been clarified until now. More importantly, the determination of explicit species and profound understanding of electron transfer pathways in interfacial region for promoting charge separation were still challenging. According to what we have known so far, unfortunately, the deep-seated studies that clearly revealed interfacial sites for boosting electron transfer in heterostructure at atomic levels were more interesting but still rarely investigated.

Herein, inspired by the synthetic protocol developed by Lou et al.[29] to deeply reveal the promotion of interfacial species on charge transfer in heterostructure channels and to solve the inefficient charge separation as well as the limited hydrogen production performance, this work gave particular emphasis to a cost-effective solution for constructing In-MOF precursors via a solvothermal reaction of $In^{3+}$ ions with organic ligand of 2-aminoterephthalic acid and then obtained the carbon-coated hollow tubular $In_2O_3$ (C/HT-$In_2O_3$), which was partially coordinated with In−N−In sites through calcining In-MOF at elevated temperature under nitrogen atmospheres. Followed with further *in situ* synthesis of thin-layered $ZnIn_2S_4$ growing on the surface of C/HT-$In_2O_3$ via a facially hydrothermal method, the hierarchical C/HT-$In_2O_3$/$ZnIn_2S_4$ heterostructure could be formed and obtained for PHE reactions from water under simulated sunlight irradiation as illustrated in Scheme 1.

## 2. EXPERIMENTAL SECTION

**2.1. Chemical Reagents.** The detailed chemical reagents related to experiments are available in Supporting Information.

**2.2. Sample Preparation.** *2.2.1. Synthesis of In-MOF.* In a typical method, 0.598 g of $In(NO_3)_3$·$4.5H_2O$ and 0.234 g of 2-aminoterephthalic acid were together added into 20 mL of DMF and stirred vigorously for 2.5 h at room temperature. The mixture was then transferred to a Teflon-lined autoclave and maintained at 125 °C for 5 h. After being cooled down to room temperature, the dark yellow solid products were filtered and washed three times with alcohol. Finally, the In-MOF samples could be obtained after vacuum drying overnight.

*2.2.2. Synthesis of C/HT-$In_2O_3$ Samples.* The above In-MOF precursors were put into a crucible and covered with aluminum foil to prevent it from floating. Followed with calcination in flow $N_2$ atmosphere for 2 h, the carbon-coated hollow tubular $In_2O_3$ samples could be obtained and donated as C/HT-$In_2O_3$ briefly. The temperature-induced (450, 500, 550 °C) carbon-coated HT-$In_2O_3$ samples were separately labeled as C/HT-$In_2O_3$-450, C/HT-$In_2O_3$-500 and C/HT-$In_2O_3$-550. For comparison, the In-MOF precursors calcined in air atmosphere were also collected and named as S−$In_2O_3$. The $In_2O_3$ samples that decomposed directly from $In(NO_3)_3$ were donated as D-$In_2O_3$, and the commercial $In_2O_3$ was abbreviated as C−$In_2O_3$.

*2.2.3. Synthesis of C/HT-$In_2O_3$/$ZnIn_2S_4$ Catalysts.* Different mass ratios of the above synthetic C/HT-$In_2O_3$ to $ZnIn_2S_4$ (1:4, 1:2, 1:1, 2:1, 4:1) were designed to prepare the composite C/HT-$In_2O_3$/$ZnIn_2S_4$ photocatalysts via a facilely hydrothermal method.[29] In detail, by using the 1:2 mass ratio of C/HT-$In_2O_3$ to $ZnIn_2S_4$ as an example, 9 mg of C/HT-$In_2O_3$ was dispersed in 8 mL of water (pH = 2.5) and 2 mL of glycerol with ultrasound treatment for 30 min and kept stirring for another 30 min. After totally being dispersed, 0.0816 g of $ZnCl_2$, 0.1758 g of $InCl_3$·$4H_2O$ and 0.09 g of thioacetamide (TAA) were sequentially added into the above dispersion and stirred vigorously for 30 min. Afterward, the mixture was placed and heated in an oil bath at 80 °C with the rate of agitator being fixed at 300 rpm. After mild agitation for 90 min, the resulting products were collected by washing two times with ethanol and drying in vacuum overnight, finally yielding targeted C/HT-$In_2O_3$/$ZnIn_2S_4$ samples.

*2.2.4. Synthesis of Comparative Samples.* The synthesis procedure of S−$In_2O_3$/$ZnIn_2S_4$, D-$In_2O_3$/$ZnIn_2S_4$, C−$In_2O_3$/$ZnIn_2S_4$ were similar to that of C/HT-$In_2O_3$/$ZnIn_2S_4$ with C/HT-$In_2O_3$ being substituted by corresponding $In_2O_3$ samples. The catalyst obtained by simply mixing C/HT-$In_2O_3$ with $ZnIn_2S_4$ was entitled as mechanical mixing sample.

**2.3. Material Characterization.** The characterization methods are supplemented in Supporting Information.

**2.4. Photocatalytic Hydrogen Evolution.** Photocatalytic hydrogen evolution (PHE) was initiated in a closed container connecting to a gas circulation externally. The light source was a 300 W Xe lamp (Perfect Light, Beijing Co., China) and the temperature was controlled at 20 °C by cooling circulating water. In detail, 5 mg of synthesized photocatalyst was added to 100 mL of deionized water containing $Na_2S$·$9H_2O$ (0.35 M) and


https://doi.org/10.1021/acscatal.0c05520
ACS Catal. 2021, 11, 6276−6289

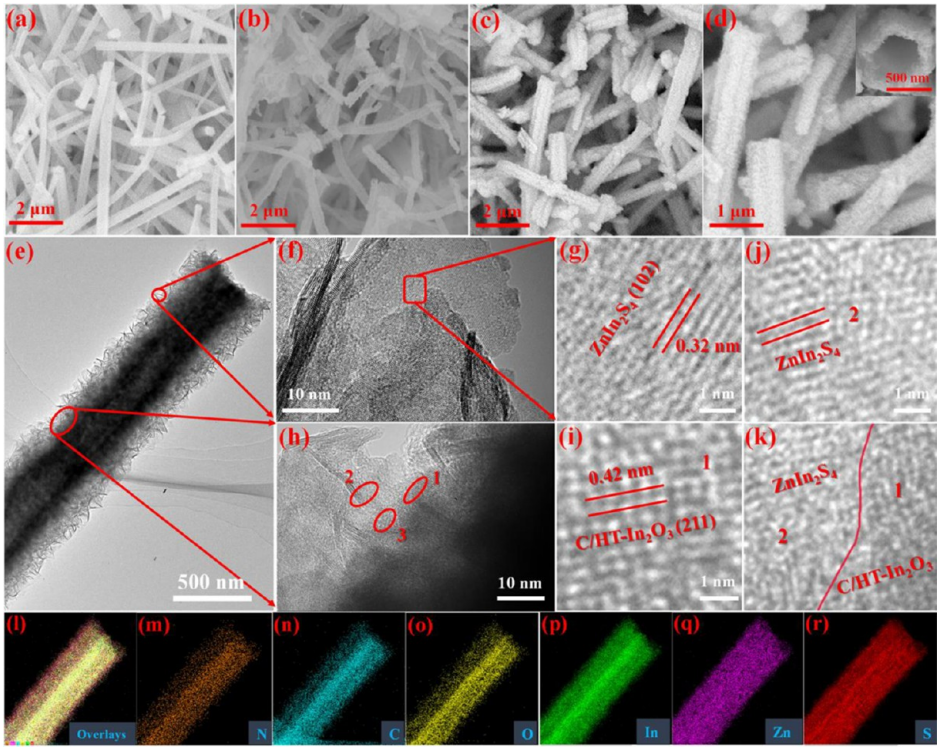


**Figure 1.** SEM images of (a) In-MOF, (b) C/HT-$In_2O_3$, (c, d) C/HT-$In_2O_3$/$ZnIn_2S_4$; (e) TEM images of C/HT-$In_2O_3$/$ZnIn_2S_4$. (f, g) HRTEM images of $ZnIn_2S_4$. (h) Heterostructure interface of C/HT-$In_2O_3$ with $ZnIn_2S_4$, the marked 1, 2, 3 ellipses represent C/HT-$In_2O_3$, $ZnIn_2S_4$ and interface, (i–k) amplified lattice distance of C/HT-$In_2O_3$, $ZnIn_2S_4$; (l–r) mapping profiles of C/HT-$In_2O_3$/$ZnIn_2S_4$ heterostructure. Note: the 1:2 proportion of C/HT-$In_2O_3$ to $ZnIn_2S_4$ was used for SEM and TEM images.

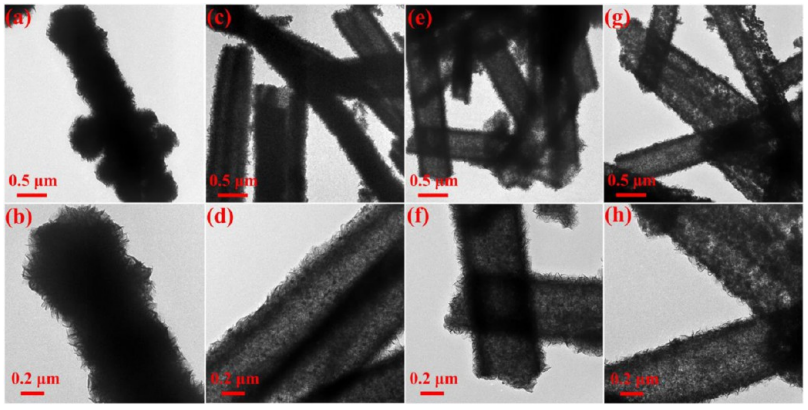


**Figure 2.** Morphology of catalyst with different proportions of C/HT-$In_2O_3$ to $ZnIn_2S_4$. (a,b) 1:4; (c,d) 1:1; (e,f) 2:1; (g,h) 4:1.

$Na_2SO_3$ (0.25 M) as sacrificial agents. Pt (2 wt%) was also employed in this system as a cocatalyst by in situ photodeposition of $H_2PtCl_6$. After it was dispersed for 30 min, the composite dispersion was transferred to a quartz reactor and evacuated by a vacuum pump. The production was sampled by extracting gases every 60 min and monitored using a gas chromatograph fitted with a 5 Å molecular sieve column and a thermal conductivity detector (TCD).

The apparent quantum efficiencies (AQEs) for photocatalytic $H_2$ evolution was measured using different monochromatic light filters (320, 350, 400, 420, 450 nm), and the AQEs were calculated according to the following equation:

$$\text{AQEs}\ (\%) = \frac{2 \times \text{number of evolved } H_2 \text{molecules}}{\text{number of incident photons}} \times 100\% = \frac{2 \times n_{H_2} \times N_A \times h \times c}{S \times P \times t \times \lambda} \times 100\%$$

where $n_{H_2}$ is the amount of $H_2$ molecules, $N_A$ is the Avogadro constant, $h$ is the Planck constant, $c$ is the speed of light, $S$ is the irradiation area, $P$ is the intensity of irradiation light which is measured by an optical power meter (CEL-NP2000, CEAULIGHT Co., Ltd.), $t$ is the photoreaction time, and $\lambda$ represents the wavelength of monochromatic light.

**2.5. EXAFS Measurement and Theoretical Calculation.** Both of these parts can be found in Supporting Information.



https://doi.org/10.1021/acscatal.0c05520
ACS Catal. 2021, 11, 6276–6289

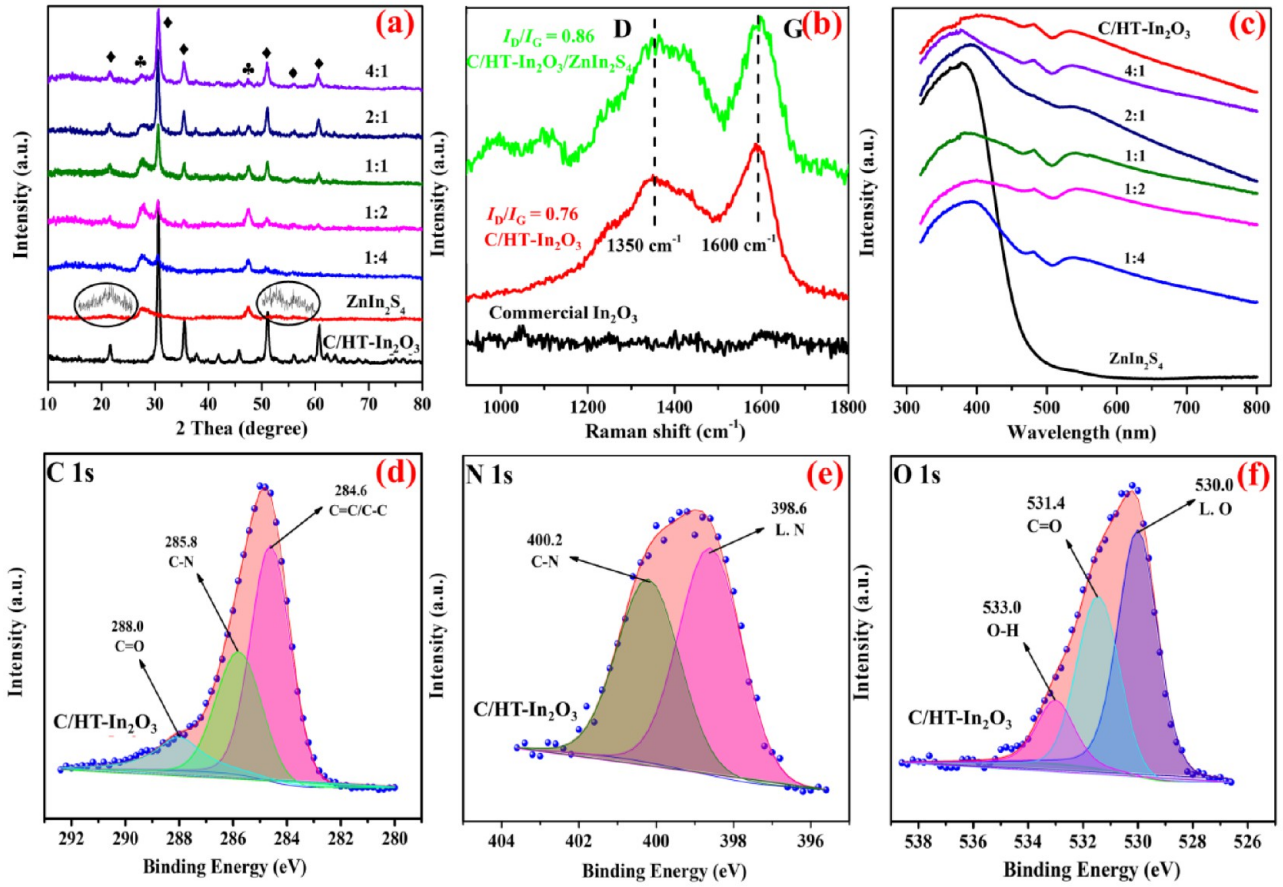


**Figure 3.** (a) XRD patterns. (b) Raman spectra. (c) UV−vis. DRS spectra of various catalysts. (d−f) High-resolution XPS spectra of C, N, O in the C/HT-$In_2O_3$ sample.

## 3. RESULTS AND DISCUSSION

**3.1. Morphology and Structure.** Scanning electron microscopy (SEM) images successfully demonstrated the solid rod of In-MOF and hollow-like structure of C/HT-$In_2O_3$ (Figure 1a,b), which was derived from the calcination treatment. After suffering a facilely hydrothermal process, it was obvious to find that both inside and outside of the C/HT-$In_2O_3$ were totally covered by thin-layered $ZnIn_2S_4$ in regular orders to rationally fabricate the targeted C/HT-$In_2O_3$/$ZnIn_2S_4$ heterostructure (Figure 1c,d). While unspecific morphology and aggregation of pristine $ZnIn_2S_4$ were observed as shown in Figure S1. Transmission electron microscope (TEM) images further proved the bolt body of In-MOF with 600 nm in width (Figure S2a,b) and C/HT-$In_2O_3$ with 500 nm in diameter (Figure S2c,d, the inset 0.42 nm lattice spacing represented the (211) crystal plane of $In_2O_3$), in which the thinner diameter might be caused by inhomogeneous shrinkage of microcrystalline during pyrolysis in nitrogen atmosphere.[30] The hierarchical structure of C/HT-$In_2O_3$/$ZnIn_2S_4$ and clustered state of pristine $ZnIn_2S_4$ discussed above were surely corroborated as shown in Figure S2e−h. Moreover, the elemental mapping distributions (Figure S3) sufficiently supported the formation of carbon-coated hollow tubular $In_2O_3$, and it was worth noting that the atomic concentration of carbon reached 30.55%, indicating organic ligand derived carbon persisted well in this hollow structure. The enlarged TEM image as shown in Figure 1e presented the spatial arrangement of the C/HT-$In_2O_3$/$ZnIn_2S_4$ heterostructure, and the marked 0.32 nm could be attributed to the (102) crystal plane of $ZnIn_2S_4$ (Figure 1f,g). The coexistence of C/HT-$In_2O_3$, $ZnIn_2S_4$, and its heterostructure interface, additionally, were circled with number 1, 2, and 3 (Figure 1h), which were further identified according to the 0.32 and 0.42 nm lattice spacing in HRTEM images (Figure 1i−k). Besides, the elemental mappings (Figure 1l−r) and EDS profiles (Figure S4) evidently confirmed the successful regulation of hierarchical carbon-coated HT-$In_2O_3$/$ZnIn_2S_4$ heterostructure.

At the same time, by managing different proportions of counterparts, the controllable morphology could also be obtained as displayed in Figure 2, indicating a feasibly applied strategy for the synthesis of the C/HT-$In_2O_3$/$ZnIn_2S_4$ heterostructure. Though the morphology of solid $In_2O_3$ (S−$In_2O_3$) that was derived from calcining In-MOF in air was basically maintained, the excessive loss of carbon in S−$In_2O_3$ was ineluctable as the atomic concentration had seriously reduced to 5.73%, which also might be responsible for the narrower diameter at about 260 nm (Figure S5). However, the thinner $In_2O_3$ was not beneficial to the formation of the heterostructure any longer, as the growing of $ZnIn_2S_4$ on its surface required a large external contact area. Thus, the corresponding S−$In_2O_3$/$ZnIn_2S_4$ composites as shown in Figure S6 barely maintained their appearance, and the heterostructure interfaces between S−$In_2O_3$ and $ZnIn_2S_4$ could not be clearly distinguished in this situation. Similar results were observed in the mechanical mixing of C/HT-$In_2O_3$ with $ZnIn_2S_4$ as shown in Figure S7−S8, and the heterostructure interfaces could not be identified at all. To clarify the effect of calcination conditions on the formation of C/HT-$In_2O_3$, thermogravimetry (TG) curves were further analyzed as shown in Figure S9−S10. The slowly


https://doi.org/10.1021/acscatal.0c05520
ACS Catal. 2021, 11, 6276−6289

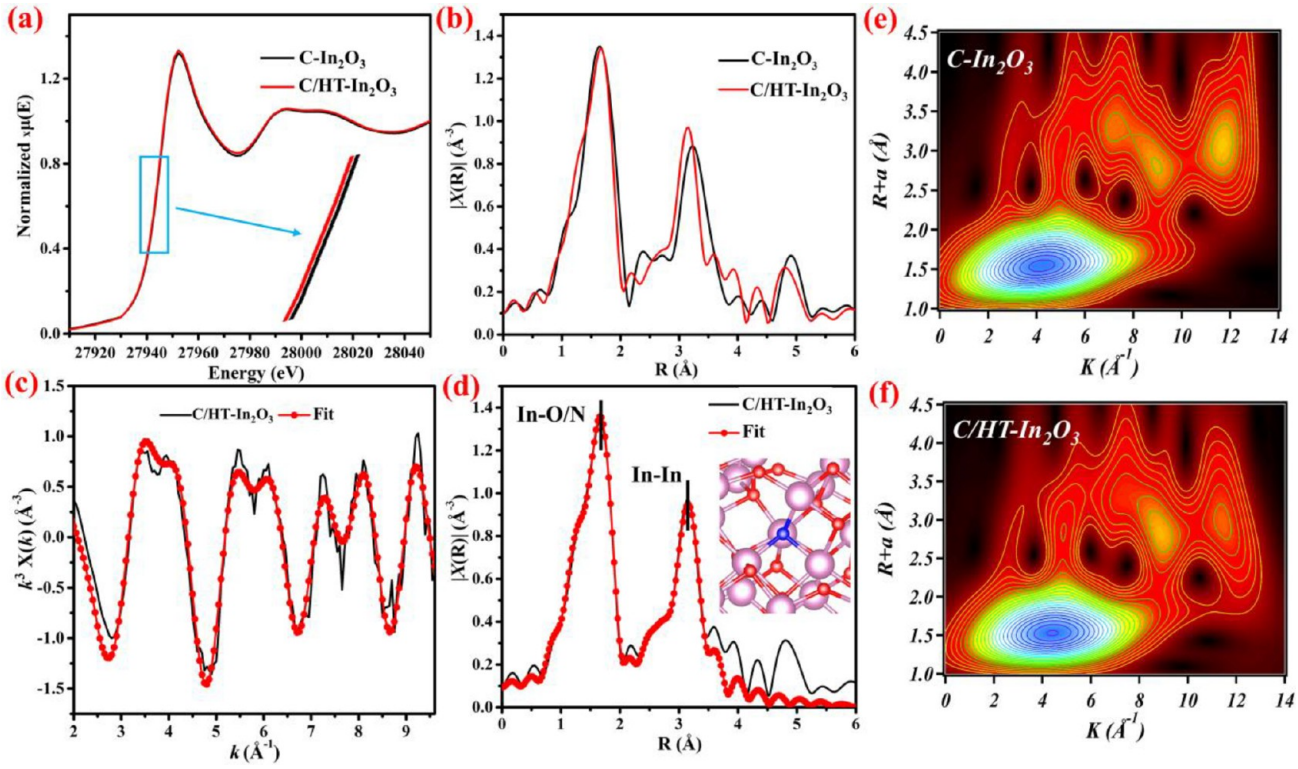


**Figure 4.** (a) Normalized XANES spectra. (b) FT-EXAFS spectra of In *K*-edge. (c,d) EXAFS fitting curves of *k* and *R* space in C/HT-$In_2O_3$; the purple balls and red balls represent In and O atoms, and the blue balls are N atoms. (e−f) Wavelet transform plots of commercial $In_2O_3$ and C/HT-$In_2O_3$.

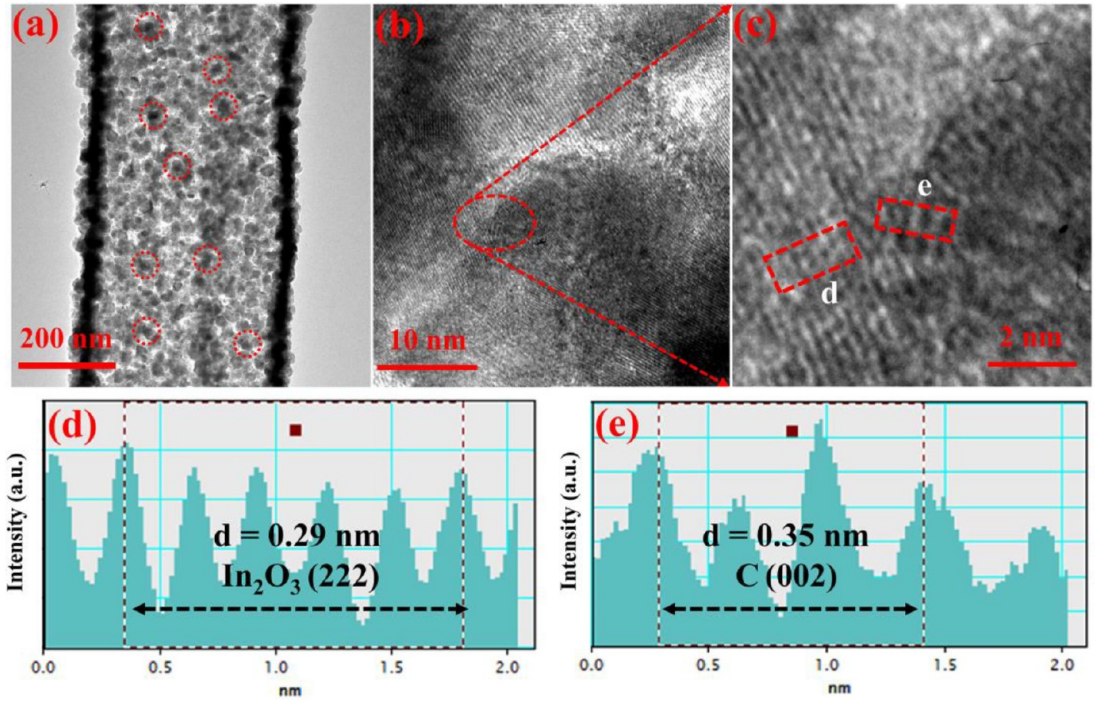


**Figure 5.** (a−c) TEM and HRTEM images to observe the distribution of carbon in the C/HT-$In_2O_3$ sample. The determined lattice space of (d) derived $In_2O_3$ and (e) partially graphitized carbon species.

changing TG and DTG curves of In-MOF in nitrogen meant a stable pyrolysis process of metal organic framework below 400 °C, indicating that the protective atmosphere was necessary to stabilize the catalyst structure with carbon coated and the required temperature to form a stable frame was about 500 °C appropriately.

XRD patterns (Figure S11) showed that the diffraction peaks at 21.5°, 30.6°, 35.5°, 51.0° and 60.7° were well consistent with (211), (222), (400), (440), (622) crystal planes of indium oxide, indicating that the cubic $In_2O_3$ was the finally resulted nanomaterial and this sample was derived from calcining In-MOF in nitrogen atmosphere. As can be seen obviously, the


https://doi.org/10.1021/acscatal.0c05520
ACS Catal. 2021, 11, 6276−6289

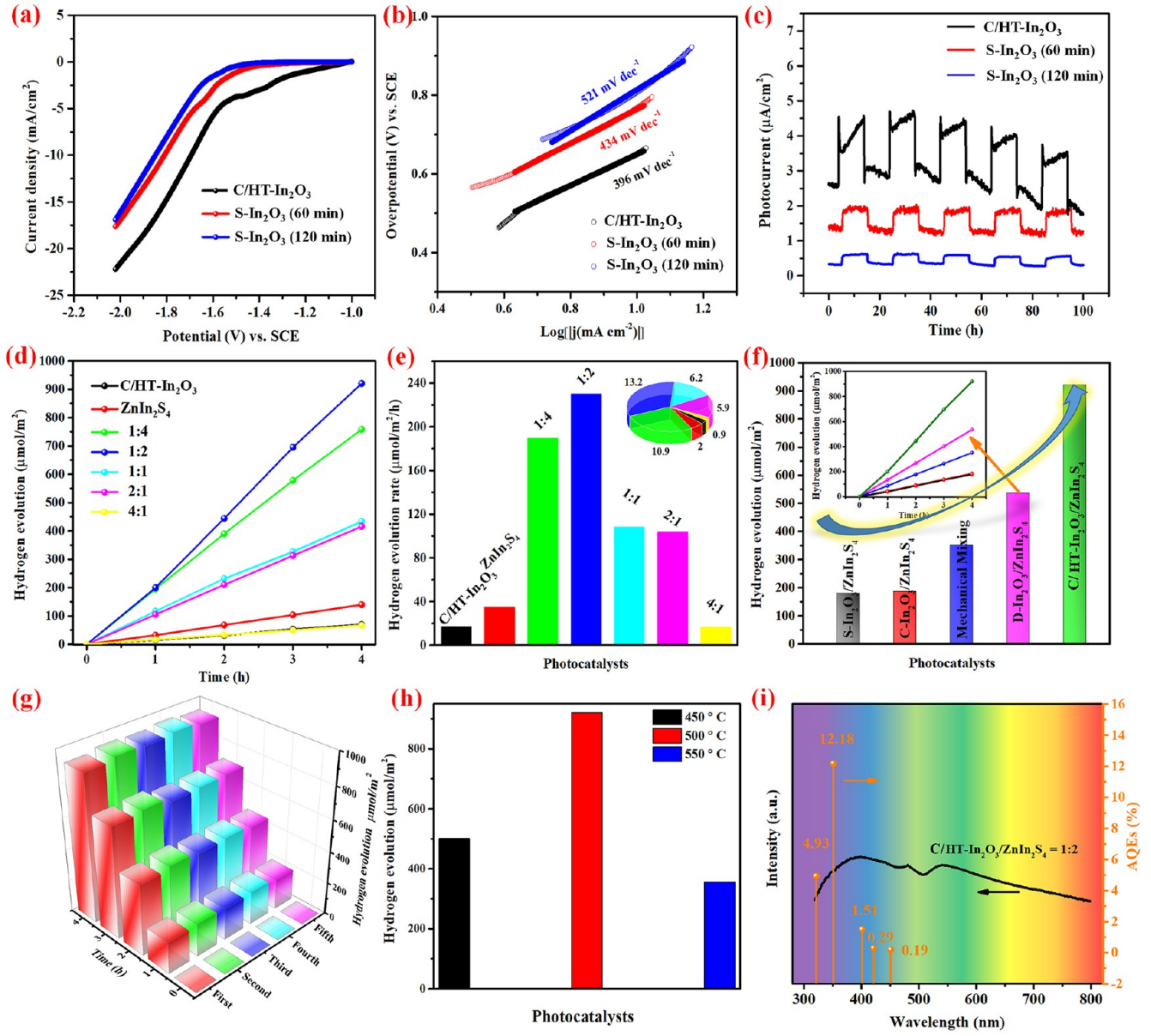


**Figure 6.** (a) LSV curves. (b) Tafel plots. (c) Photocurrent response of C/HT-$In_2O_3$ and S−$In_2O_3$ samples. (d) Time-dependent curves of $H_2$ evolution. (e) $H_2$ evolution rate with gradient proportions of the counterpart in catalysts. (f) $H_2$ generation activity of comparative samples. (g) Cycle stability test. (h) Temperature-dependent induced C/HT-$In_2O_3$ coupling with $ZnIn_2S_4$ (1:2) catalysts for $H_2$ generation. (i) Apparent quantum efficiencies under 320, 350, 400, 420, and 450 nm at monochromatic light.

appeared peaks at 21.6°, 27.7°, 47.2°, 52.4°, and 55.6° corresponded well to (006), (102), (110), (116), and (022) crystal planes of hexagonal $ZnIn_2S_4$,[31,32] and were all displayed in C/HT-$In_2O_3$/$ZnIn_2S_4$ accompanied with cubic $In_2O_3$ (Figure 3a). The enhanced peak intensity of C/HT-$In_2O_3$ was clearly observed with an increase in the proportion, suggesting the successful synthesis of a heterostructure with high crystallinity. Raman spectra demonstrated the partially graphitized carbon in C/HT-$In_2O_3$ as the intensity of the D band was weaker than that of the G band (Figure 3b) and graphitized carbon had been widely reported to facilitate electron transfer, leading to an enhanced photocatalytic reaction.[33−35] However, the increased $I_D/I_G$ value of C/HT-$In_2O_3$/$ZnIn_2S_4$ (1:2) implied a slight damage to the graphitized carbon in simply hydrothermal synthesis process. The optical properties (Figure 3c) illustrated a superior light absorption capacity of carbon-coated HT-$In_2O_3$, and the optical performance of C/HT-$In_2O_3$/$ZnIn_2S_4$ heterostructure was largely affected by the different mass proportions of components, in which gradually elevated contents of C/HT-$In_2O_3$ tended to promote stronger light absorption capacity of a heterostructure because of the increased carbon contents,[36] whereas too much carbon in C/HT-$In_2O_3$ might be useless to boost photocatalytic reaction because of the blocked carrier flow process.[37] The XPS survey spectra (Figure S12) revealed the existence of Zn, In, S, O, N elements, and the high-resolution XPS spectra of C and N in C/HT-$In_2O_3$ are shown in Figure 3d,e. The binding energies located at 284.6, 285.8, and 288.0 eV of C 1s could be attributed to the contaminated carbon, C−N bond, and C═O bond,[38] while the divided peaks at 398.6 and 400.2 eV of N 1s were assigned to lattice N and C−N bond.[39] Though the similar binding energy position of N 1s in the XPS spectrum could be found at ca. 398.6 eV,[40,41] the main $In_2O_3$


https://doi.org/10.1021/acscatal.0c05520
ACS Catal. 2021, 11, 6276−6289

**Table 1. Comparison of the Photocatalytic Activity of C/HT-$In_2O_3$/$ZnIn_2S_4$ Sample with Different Catalysts for $H_2$ Production under Simulated Sunlight Irradiation**

| catalysts | overall $H_2$ evolution ($\mu$mol/g)[a] | overall $H_2$ evolution ($\mu$mol/$m^2$)[b] | $S_{BET}$ ($m^2$/g)[c] |
|---|---|---|---|
| $ZnIn_2S_4$ | 12314 | 139.6 | 88.2 |
| C/HT-$In_2O_3$ | 3406 | 69.5 | 49.0 |
| C/HT-$In_2O_3$/$ZnIn_2S_4$ (1:4) | 26462 | 758.2 | 34.9 |
| C/HT-$In_2O_3$/$ZnIn_2S_4$ (1:2) | 37466 | 920.5 | 40.7 |
| C/HT-$In_2O_3$/$ZnIn_2S_4$ (1:1) | 52400 | 433.1 | 121.0 |
| C/HT-$In_2O_3$/$ZnIn_2S_4$ (2:1) | 47684 | 415.7 | 114.7 |
| C/HT-$In_2O_3$/$ZnIn_2S_4$ (4:1) | 6288 | 67.3 | 93.5 |
| D-$In_2O_3$/$ZnIn_2S_4$ | 12576 | 535.1 | 23.5 |
| C−$In_2O_3$/$ZnIn_2S_4$ | 14408 | 184.5 | 78.1 |
| mechanical mixing | 18080 | 350.4 | 51.6 |
| S−$In_2O_3$/$ZnIn_2S_4$ | 30360 | 177.5 | 171.0 |
| C/HT-$In_2O_3$-450/$ZnIn_2S_4$ | 38776 | 500.9 | 77.4 |
| C/HT-$In_2O_3$-550/$ZnIn_2S_4$ | 34322 | 356.4 | 96.3 |

[a]Overall $H_2$ amount produced after 4 h of light irradiation per unit mass of catalyst. [b]Overall $H_2$ amount produced after 4 h of light irradiation per unit surface area of catalyst. [c]Measured BET surface area.

containing system was totally different from the reported In oxynitrides and InN substances as confirmed by the above XRD patterns. The attributable peaks of C 1s and N 1s in C/HT-$In_2O_3$ samples initially certificated the coexistence of lattice N atoms and coated carbon species, which were all expected to be from In-MOF precursor and fixed in hollow tubular $In_2O_3$ during pyrolysis. Moreover, the O 1s spectra (Figure 3f) mainly consisted of lattice O (530.0 eV), C═O (531.4 eV), and O−H group (533.0 eV), which might come from the adsorbed surface water molecules.[42,43] After coupling with the $ZnIn_2S_4$ thin-layer, unapparent binding energy shifts of Zn 2p, In 3d, and S 2p were observed (Figure S13), confirming a stable surface chemical composition of the as-prepared C/HT-$In_2O_3$/$ZnIn_2S_4$ (1:2) heterostructure.

**3.2. Determination of Coordinated In−N−In Sites.** To accurately confirm the local species in C/HT-$In_2O_3$, the corresponding hard X-ray absorption near-edge structure (XANES) and extended X-ray absorption fine structure (EXAFS) were investigated. Results showed that unobvious changes of XANES spectra between commercial $In_2O_3$ (C−$In_2O_3$) and C/HT-$In_2O_3$ were observed as exhibited in Figure 4a, while EXAFS clearly revealed a different coordinated structure of C−$In_2O_3$ and C/HT-$In_2O_3$ (Figure 4b, Figure S14−S15). For C/HT-$In_2O_3$, the fitting results in *K* and *R* space (Figure 4c,d) were further analyzed, and the first peak of *R* space in EXAFS curve could be cocontributed by dominant In−O and In−N coordinated species at about ∼1.65 Å. The detailed fitting parameters are listed in Tables S1−S2. Wavelet transform (WT) EXAFS plots (Figure 4e,f) also demonstrated the signal of coordinated In−N sites in C/HT-$In_2O_3$ in comparison with that of the other counterpart. These results all brought insight into the local structural of In species at the atomic level that were coordinated by both O and N atoms in C/HT-$In_2O_3$, which were in good agreement with XPS analysis. Combining the coordinated In−N sites with the above evidence had confirmed the existence of lattice N in C/HT-$In_2O_3$ samples by the determination of XPS results; thus, the In−N−In sites could be subsequently proposed. What's more, the microporous structure with a large surface area of In-MOF (483 $m^2$ $g^{-1}$) is presented in Figure S16, providing energetic advantages for the homogeneous formation of In−N−In sites dispersing in hollow tubular structure. Notably, the seriously reduced surface area of C/HT-$In_2O_3$ (49 $m^2$ $g^{-1}$) indicated a damaged pore structure of In-MOF in pyrolysis process (Figure S17), and the increased surface area of C/HT-$In_2O_3$/$ZnIn_2S_4$ might be caused by the regular arrangement of thin-layered $ZnIn_2S_4$ flakes as proved in Figure S18.

**3.3. Revelation of Carbon Species.** The potential function of carbon in this system was another important aspect that is worthy to be investigated because a large percentage of carbon content (30.55%) had been confirmed in the as-prepared C/HT-$In_2O_3$. Though the characteristic XRD diffraction peak of carbon in C/HT-$In_2O_3$ did not appear, the partially graphitized carbon had been indeed confirmed on the basis of the above Raman analysis. Moreover, the random distribution of carbon and observation of the lattice space of partially graphitized carbon around $In_2O_3$ samples as marked in Figure 5 strongly proved the formation of carbon species accompanied with the stabilization of In−N−In sites in the pyrolysis process. However, the EXAFS result did not expose any carbon atoms that were linked to In clusters in C/HT-$In_2O_3$ samples. Therefore, based on the evidence collected so far, the main existence of coated carbon was still a large number of amorphous state that stacked randomly. From the perspective of material synthesis, the stacked carbon maintained the necessary diameter of C/HT-$In_2O_3$ for the growth of crystal $ZnIn_2S_4$ because the thicker tube might not provide enough grasping surface to equalize the distribution of $ZnIn_2S_4$, leading to a redundant coated $ZnIn_2S_4$ mode as shown in Figure S19. The function of carbon on material synthesis was one aspect, but more importantly, the high electric conductivity of carbon was decisive as it had been widely investigated and reported for promoting the separation and transfer of photogenerated charge carriers in boosting photocatalytic activity.[44,45]

**3.4. Photoelectrochemical Activity and Photocatalytic Hydrogen Evolution Performance.** To objectively evaluate the promotion of carbon on charge migration, the photoelectrochemical activity of different S−$In_2O_3$ samples that calcined In-MOF in air for 60 and 120 min were investigated and compared with that of C/HT-$In_2O_3$. Under simulated sunlight irradiation, the optimum linear sweep voltammetry (LSV) curves of C/HT-$In_2O_3$ samples (Figure 6a) illustrated the considerable transfer and separation of photoinduced carriers than S−$In_2O_3$,[46] in which the current density was gradually decreased with carbon burned away, proving the importance of carbon for the transmission of electrons to participate in the reduction of water to hydrogen. Similar results were also observed in the Tafel slope as shown in Figure 6b, where with the assistance of carbon for electron migration, a slope of C/HT-$In_2O_3$ catalyst was calculated at 396 mV $dec^{-1}$, smaller than the other S−$In_2O_3$ catalysts, confirming the benefits of conductive carbon to electron migration for hydrogen evolution.[47] In addition, the comparison of photocurrent curves (Figure 6c) fully gave a positive support to the above conclusion. In general, the derived carbon accelerated the charge-transfer efficiency as an electronic transmission bridge in C/HT-$In_2O_3$ samples, resulting in an enhanced photoelectrochemical activity.

Though lots of determination of photocatalytic hydrogen evolution (PHE) rates with per mass of catalyst as unit had been reported, the relationship between PHE rates and mass of catalysts was not necessarily linear, and the geometric effects might also contribute to the reactions, which could not


https://doi.org/10.1021/acscatal.0c05520
ACS Catal. 2021, 11, 6276−6289

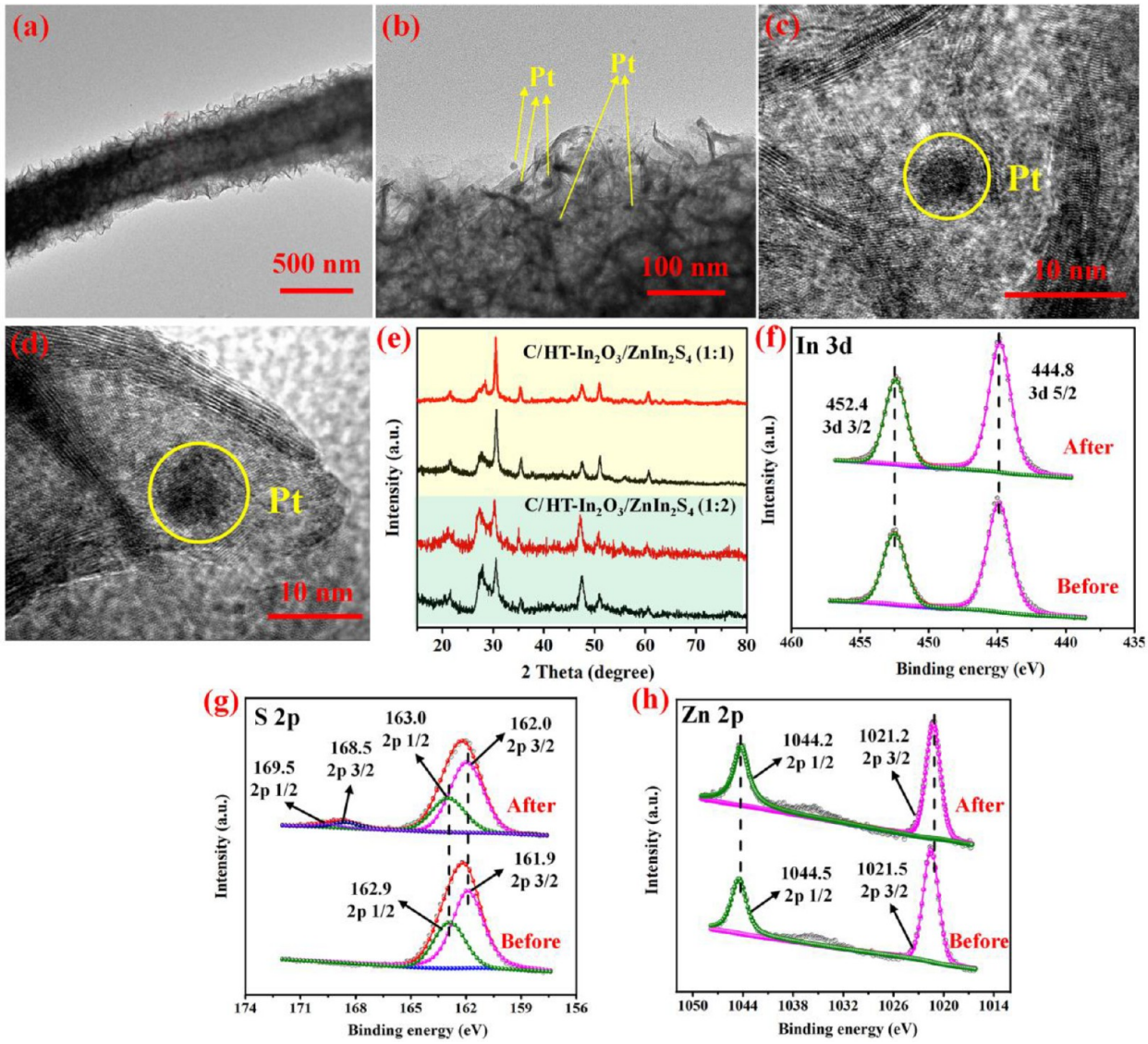


**Figure 7.** TEM images of (a) used C/HT-$In_2O_3$/$ZnIn_2S_4$ (1:2). (b–d) Observation of deposited Pt nanoparticle. (e) XRD patterns of fresh (black line) and used (red line) photocatalysts. (f–h) High-resolution XPS spectra of In, S, Zn after recycling over C/HT-$In_2O_3$/$ZnIn_2S_4$ (1:2).

accurately measure the actual efficiency of the catalyst anymore.[48,49] To express with a more scientific way, the PHE performance was thoroughly normalized by measuring the surface area of the catalysts.[50,51] The apparent observation of a series of comparative catalysts were shown in Figure S20, and the nitrogen sorption isotherms of various catalysts were supplemented in Figures S21–S22. It could be seen that the pristine $ZnIn_2S_4$ played a dominant catalyst in photocatalytic hydrogen generation, giving an evolution of 139.6 $\mu$mol/$m^2$ during 4 h of reaction, while for pristine C/HT-$In_2O_3$, only an amount of 69.5 $\mu$mol/$m^2$ of $H_2$ was released (Figure 6d). Nonetheless, a substantially increased PHE rates was achieved after constructing the C/HT-$In_2O_3$/$ZnIn_2S_4$ heterostructure (1:2), bringing to an amount of 230.1 $\mu$mol/$m^2$/h at the highest level for hydrogen evolution, about 6.6 and 13.2 times higher than that of pristine $ZnIn_2S_4$ and C/HT-$In_2O_3$ (set as base 1), respectively (Figure 6e). Comparison of PHE performance with reported literatures was summarized in Table S3, illustrating the superior photocatalytic activity among $ZnIn_2S_4$-based materials. In addition, the mass ratio of C/HT-$In_2O_3$ in heterostructure regularly affected the PHE reactions and the difference of catalytic activity caused by gradient ratio of C/HT-$In_2O_3$ could be analyzed according to the morphologic diversity (Figure 2), in which thickly covered $ZnIn_2S_4$ prevented C/HT-$In_2O_3$ from being irradiated and stimulated, meaning a nearly single component of $ZnIn_2S_4$ acted on this occasion rather than a heterostructure. On the contrary, a small amount of $ZnIn_2S_4$ seriously reduced the catalytic activity because it was the main active substrate for the trigger of PHE reactions. Meanwhile, the PHE performance of several comparative samples were also investigated as shown in Figure 6f, demonstrating the superior activity of the targeted C/HT-$In_2O_3$/$ZnIn_2S_4$ heterostructure. A cyclic stability test of C/HT-$In_2O_3$/$ZnIn_2S_4$ (1:2) without any sacrificial supply was also evaluated by operating reactions for successive five cycles, and the steadily increased hydrogen evolution curves with little fluctuation showed an excellent hydrogen evolution ability (Figure 6g). More importantly, the PHE activity of C/HT-$In_2O_3$/$ZnIn_2S_4$ (1:2) in a real water environment was also estimated, and an obvious hydrogen production in tap and river water bodies was subsequently exhibited (Figures S23–S25), all confirming a potential promising catalyst of the as-prepared C/HT-$In_2O_3$/$ZnIn_2S_4$. It


https://doi.org/10.1021/acscatal.0c05520
ACS Catal. 2021, 11, 6276–6289

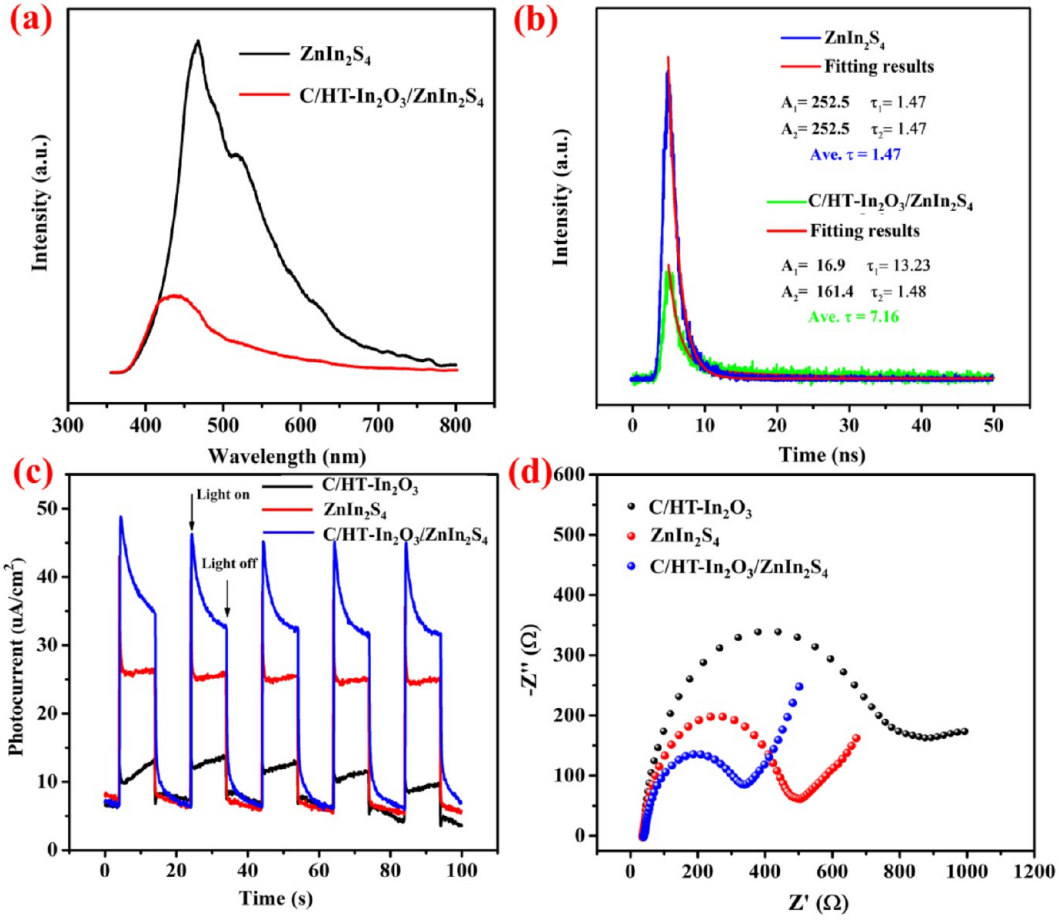


**Figure 8.** (a) Steady-state PL spectra. (b) Time-resolved PL spectra. (c) Transient photocurrent responses. (d) EIS Nyquist plots of synthesized photocatalysts. Note: the proportion of C/HT-$In_2O_3$ to $ZnIn_2S_4$ was set at 1:2.

was noted that different calcination-temperature-induced C/HT-$In_2O_3$ affected PHE performance distinctly after coupling with $ZnIn_2S_4$, as exhibited in Figure 6h. Possible reasons might be ascribed to the different amount of formed In−N−In sites that had anchored in C/HT-$In_2O_3$ within the temperature range. Additionally, the selectivity of C/HT-$In_2O_3$/$ZnIn_2S_4$ (1:2) to sacrificial agent was thoroughly examined, and results showed that the weak alkaline benefited a lot (Figure S26). As a conclusion, to be more intuitive, all the overall photocatalytic $H_2$ evolution activities both with the unit of $\mu$mol/g and $\mu$mol/$m^2$ are shown in Table 1, where indeed it is illustrated that the highest catalytic $H_2$ efficiency per mass of catalysts did not mean the strongest focus spot with the unit of per surface area. Furthermore, the almost positive correlation between PHE performance and wavelength of incident light proved that the stronger light absorption intensity would excite more carriers and led to a higher catalytic activity as shown in Figure 6i. It was also noted that the apparent quantum efficiency (AQE) was largely affected by the wavelength of incident light, and the optimized AQE at 350 nm ran up to 12.18%, a relatively high value in $ZnIn_2S_4$ composites until now (Tables S3−S4). However, the lower AQE in the ultraviolet region would be associated with the natural characteristics of catalyst that mainly responded under visible light, and the inactive state of catalysts in the wavelength beyond 420 nm might be caused by the insufficient light energy utilization. On the whole, the $H_2$ generation activity, together with the higher reported AQE value, signified a useful catalyst of C/HT-$In_2O_3$/$ZnIn_2S_4$ for photocatalytic reactions.

**3.5. Stability Test of Photocatalysts.** The recycling of the catalyst was an important part of stability assessment;[52,53] thus, the property testing experiments of C/HT-$In_2O_3$/$ZnIn_2S_4$ after utilization were further conducted by observing morphology, XRD patterns and XPS spectra. First of all, the change of morphology was one of the most direct indicators to reflect the stability of photocatalyst. The retained hierarchically hollow tubular heterostructure, therefore, indicated inconspicuous morphology changes before and after use (Figure 7a), proving the structural stability of the as-synthesized photocatalysts for PHE reactions. Besides, the clear observation of Pt nanoparticles that deposited on the surface of $ZnIn_2S_4$ thin-layer (Figure 7b−d, Figure S27) further favored the effective reduction of protons to hydrogen and boosted PHE performance due to the more provided photocatalytic center sites.[54] The observation and statistically significant diameter of deposited Pt nanoparticles on the surface of $ZnIn_2S_4$-based catalysts were proved to be similar at about 7−8 nm as shown in Figure S28, indicating that the improvement of catalytic performance was originated from the microstructure of the catalyst itself, not the size and distribution of the Pt cocatalyst. The recovered crystal composition could also be useful to measure the stability of catalysts; however, the insignificant XRD patterns revealed the perfectly reserved crystallinity of used C/HT-$In_2O_3$/$ZnIn_2S_4$ as shown in Figure 7e, demonstrating the superior stability of the as-prepared photocatalysts. Furthermore, XPS spectra of In 3d, S 2p, Zn 2p


https://doi.org/10.1021/acscatal.0c05520
ACS Catal. 2021, 11, 6276−6289

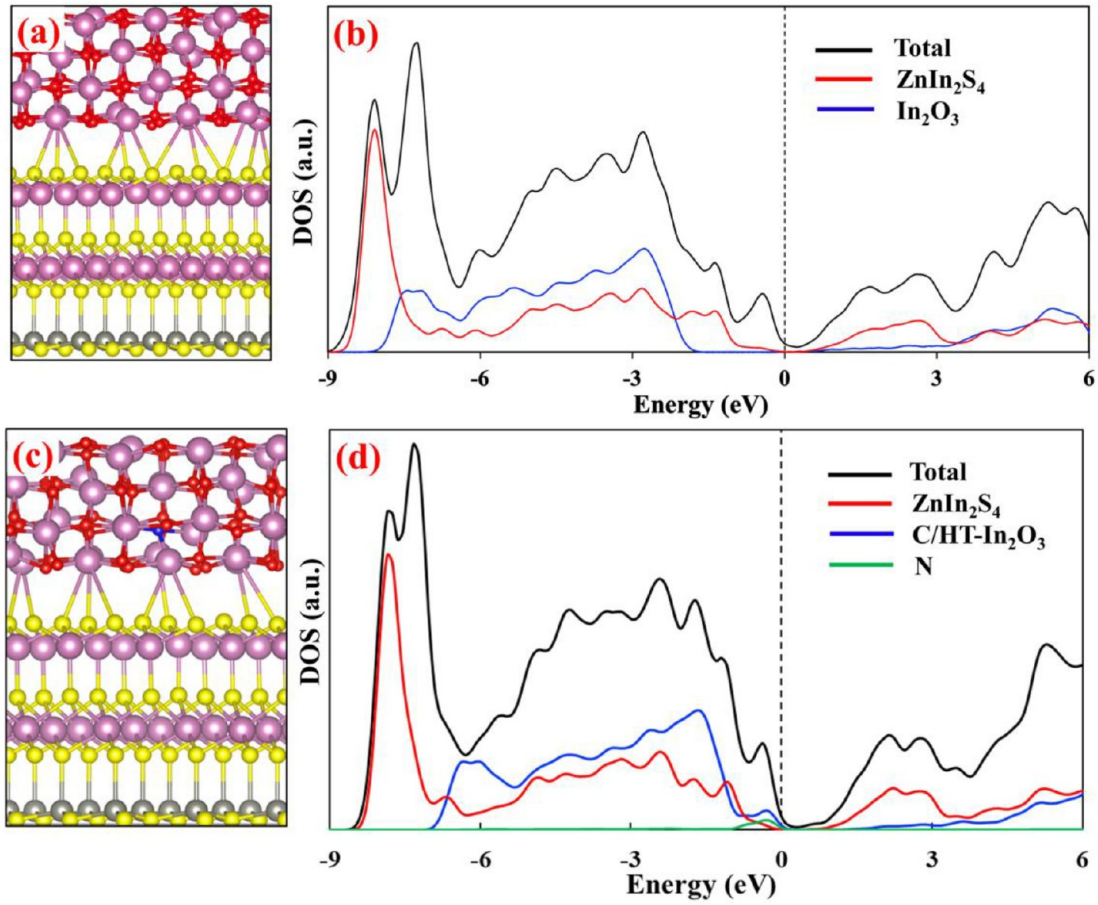


**Figure 9.** (a,c) Atomically fabricated structures. (b,d) Density of states (DOS) for the $In_2O_3/ZnIn_2S_4$ and C/HT-$In_2O_3/ZnIn_2S_4$ heterostructures. The Fermi level of the heterostructure was set as the reference zero. Colors in (a,c): purple balls are In; yellow balls are S; gray balls are Zn; red balls are O; blue balls are N. Colors in (b,d): Black line is total DOS; red line is projected DOS (PDOS) of $ZnIn_2S_4$; blue line is PDOS of $In_2O_3$ or C/HT-$In_2O_3$; green line is PDOS of N. The magnitude of PDOS for $In_2O_3$, C/HT-$In_2O_3$, and N is amplified by 3 fold.

(Figure 7f–h) released a similar peak signal without obvious decline in comparison with that of the fresh catalysts, in which the weak peak emerged at around 169 eV of S 2p spectra could be well ascribed to the oxidized state of $SO_4^{2-}$ that came from the sacrificial agent, guaranteeing a stable chemical composition environment in the heterostructure. These results all synthetically supported the superior stability of the C/HT-$In_2O_3$/$ZnIn_2S_4$ heterostructure after suffering long-time PHE cyclic utilization.

**3.6. The Investigation of Charge-Transfer Behaviors.** To deeply reveal the charge separation/recombination efficiency of different samples, the photoelectrochemical characterizations were correspondingly carried out. According to the principle of solid state photoluminescence (PL), the more photogenerated electrons and holes combined, the stronger the fluorescence signal would be.[55] Thus, the decreased steady-state PL spectrum of the heterostructure indicated an effectively blocked recombination of charge carriers in comparison with pristine $ZnIn_2S_4$ (Figure 8a). Moreover, the charge-carrier decay dynamics of C/HT-$In_2O_3/ZnIn_2S_4$ (Figure 8b) displayed an average lifetime of 7.16 ns, which was longer than that of pure $ZnIn_2S_4$ (1.47 ns) based on the fitting results, further proving the less recombination and faster charge separation efficiency.[56,57] The investigation of charge transfer was also examined by the behavior of photocurrent under simulated sunlight irradiation.[58] The strongest photocurrent response during five light-on and light-off cycles caused by the rapidly transient charge transfer confirmed the optimal capability for separating carriers of heterostructure as shown in Figure 8c. Additionally, the smallest semicircle Nyquist plots (Figure 8d) induced by lower resistance for charge migrating intuitively demonstrated an accelerated charge transfer of C/HT-$In_2O_3/ZnIn_2S_4$ heterostructure,[59,60] while the large arc radius reflected the poor performance of a single component for electron transmission. These photoelectrochemical results all identically revealed the significantly inhibited recombination of charger behaviors and fast transfer efficiency, resulting in an enhanced photocatalytic performance, which was consistent with the hydrogen evolution results.

**3.7. Theoretical Calculation.** To obtain the band alignment, the atomic structure and density of states (DOS) of $In_2O_3/ZnIn_2S_4$ and C/HT-$In_2O_3/ZnIn_2S_4$ heterostructure were additionally calculated according to density functional theory (DFT) method. Using our recently developed interface prediction method,[61] we first constructed the $In_2O_3/ZnIn_2S_4$ heterostrucure and investigated the electronic structures, as shown in Figure 9a. To model the interface, we glued two slab models consisting of 0.5 nm $In_2O_3$ and 2 nm $ZnIn_2S_4$ layers in a surface supercell with dimensions 10.40 × 14.09 $Å^2$; altogether, this corresponded to 234 atoms per unit cell. The orientation relationships of the $In_2O_3/ZnIn_2S_4$ heterostructure were $(110)_{In2O3}//(001)_{ZnIn2S4}$. Both $ZnIn_2S_4$ and $In_2O_3$ were semiconductors, with bandgaps of 0.7 and 2.5 eV, respectively. The


https://doi.org/10.1021/acscatal.0c05520
ACS Catal. 2021, 11, 6276–6289

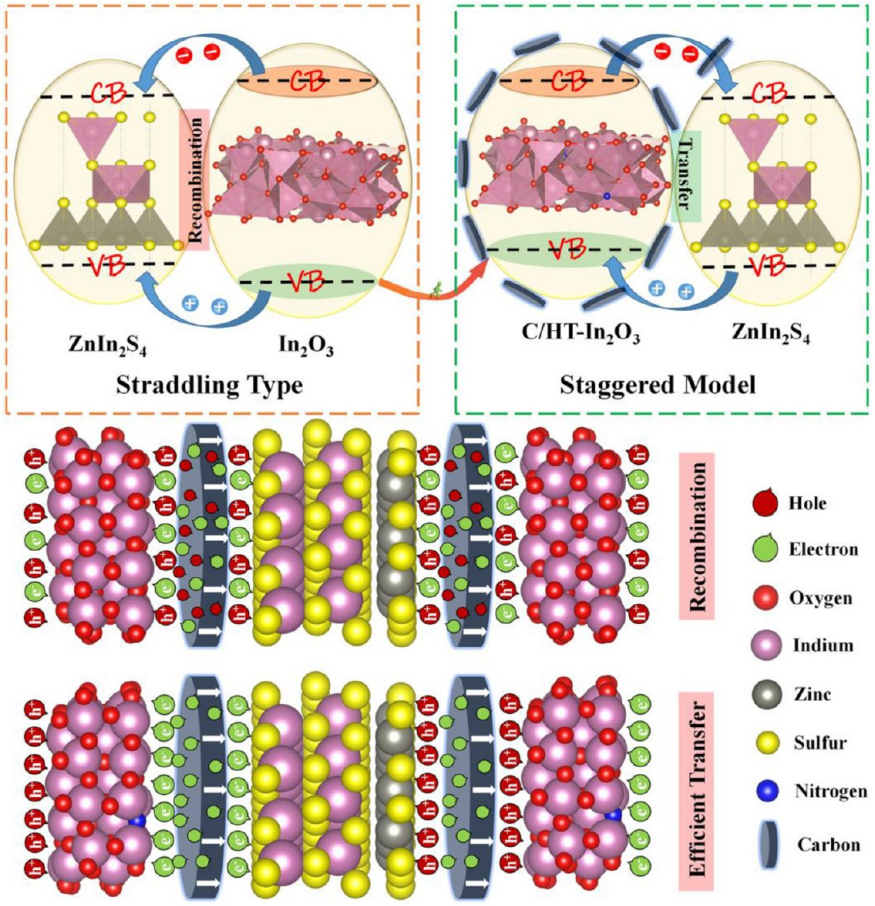


**Figure 10.** Illustration of the formation mechanism of staggered C/HT-$In_2O_3$/$ZnIn_2S_4$ heterostructure and possibly smooth interfacial charge-transfer pathways.

density of states (DOS) in Figure 9b showed that the valence band maximum (VBM) and conduction band minimum (CBM) of $ZnIn_2S_4$ were −0.2 and 0.5 eV relative to the Fermi level, while VBM and CBM of $In_2O_3$ were −1.8 and 0.6 eV relative to the Fermi level. As a result, the $In_2O_3$/$ZnIn_2S_4$ heterostructure had a Type-I straddling gap. Next, we investigated the electronic structures of C/HT-$In_2O_3$/$ZnIn_2S_4$ as shown in Figure 9c,d. In the C/HT-$In_2O_3$, 2% O atoms were replaced by N. Our results showed that $ZnIn_2S_4$ had a bandgap of 0.8 eV, similar to that in pure $In_2O_3$/$ZnIn_2S_4$. However, C/HT-$In_2O_3$ had a new peak around the Fermi level, which decreased its bandgap to 1.8 eV, smaller than that in pure $In_2O_3$/$ZnIn_2S_4$ heterostructure (i.e., 2.5 eV). More importantly, the band diagram of C/HT-$In_2O_3$/$ZnIn_2S_4$ changed to a type-II staggered gap, where VBM of C/HT-$In_2O_3$ was higher than that of $ZnIn_2S_4$. These results indicated that the lattice In−N−In sites not only induced the narrow band gap of C/HT-$In_2O_3$ (Figure S29) but also favored the formation of staggered heterostructure for boosting charge separation.

**3.8. Possible Photocatalytic Mechanism.** From the aspects of experimental results, to understand the conduction band (CB) of C/HT-$In_2O_3$ and $ZnIn_2S_4$, a Mott−Schottky plot of each counterpart was acquired as shown in Figure S30. Usually about 0.2 V difference between SCE and normal hydrogen electrode (NHE) existed;[62] thus, the accurate CB of C/HT-$In_2O_3$ and $ZnIn_2S_4$ was predicted to be −0.71 and −0.51 V, which all met the potential requirement of reducing $H^+$ to hydrogen. To make clear the valence band (VB) of C/HT-$In_2O_3$ and $ZnIn_2S_4$, valence-band XPS spectra as well as Kubelka−Munk conversion were analyzed.[63,64] The valence band (VB) of C/HT-$In_2O_3$ was then estimated at 1.90 V according to $E_{NHE}/V = \Phi + 2.51\ eV - 4.44$[65] ($E_{NHE}$: potential of normal hydrogen electrode and $\Phi$ of 3.83 eV: the electron work function of the analyzer) and the band gap of $ZnIn_2S_4$ was about ∼2.46 eV as shown in Figure S31. Therefore, the specifically matched band structure of C/HT-$In_2O_3$/$ZnIn_2S_4$ and possible transfer pathways of photoinduced carriers are displayed in Figure S32, consisting well with the computational results. Putting these theoretical and experimental results together, the possible photocatalytic mechanism for boosting interfacial charge transfer and enhancing hydrogen evolution was eventually proposed as exhibited in Figure 10. The excited carriers all migrated from $In_2O_3$ to $ZnIn_2S_4$ as observed in straddling heterostructure upon light irradiation, and this kind of moving path in the same direction failed to promote the separation of charges, leading to an aggravated recombination and reduced photocatalytic performance in the $In_2O_3$/$ZnIn_2S_4$ photocatalyst. On the contrary, with a narrowed valence band of C/HT-$In_2O_3$ by In−N−In sites anchored in the heterostructure of C/HT-$In_2O_3$/$ZnIn_2S_4$, a model of photocatalytic mechanism had turned to a staggered one, and this bidirectional transfer pathway favored the fast separation of electrons and hole pairs as much as possible when reactions occurred, resulting in the boosted interfacial charge transfer and enhanced photocatalytic hydrogen evolution performance understandably. Besides, on the basis of stronger electron donating ability of In−N−In sites and high


https://doi.org/10.1021/acscatal.0c05520
ACS Catal. 2021, 11, 6276−6289

electronic conduction of carbon for charge separation from C/HT-$In_2O_3$ to $ZnIn_2S_4$, the smooth distribution and conducive transfer of carriers at the interface of heterostructure were also responsible for the enhancement of photocatalytic activity.

## 4. CONCLUSIONS

In summary, a hierarchically C/HT-$In_2O_3$/$ZnIn_2S_4$ heterostructure was directionally fabricated by growing $ZnIn_2S_4$ thin-layer on the carbon-coated hollow tubular $In_2O_3$ (C/HT-$In_2O_3$) as targeted catalyst for photocatalytic hydrogen generation. On one hand, the particular structure of C/HT-$In_2O_3$ derived from In-MOF retained coordinated composition of In−N−In species, which deduced narrow band gap of $In_2O_3$ and favored the formation of staggered heterostructure for boosting charger transfer between C/HT-$In_2O_3$ and $ZnIn_2S_4$. On the other hand, the high electronic bridge function of carbon for promoting charge separation from C/HT-$In_2O_3$ to $ZnIn_2S_4$ counterpart further accelerate the protonation process, synergistically resulting in a significant promotion of photocatalytic hydrogen evolution performance. However, the detailed effect of temperature-induced composition and amount of In−N−In sites on improving the photocatalytic performance was still in progress.

## ■ ASSOCIATED CONTENT

### Supporting Information

The Supporting Information is available free of charge at https://pubs.acs.org/doi/10.1021/acscatal.0c05520.

Additional details on chemical reagents, materials characterization, theoretical calculation methods; SEM images, TEM images, EDS spectra, mapping profiles; TG and DTG curves; XRD patterns; higher resolution of XPS spectra; EXAFS fitting parameters and results; $N_2$ adsorption−desorption isotherms; photocatalytic hydrogen production in tap and river water; effect of sacrificial agents on photocatalytic performance; narrowed band gap of C/HT-$In_2O_3$ by In−N−In sites; Mott−Schottky plots; Valence-band XPS spectra; schematic illustration of transfer pathways of photogenerated carriers; comparison of photocatalytic hydrogen evolution with reported literatures; summarized data for AQE calculation (PDF)

## ■ AUTHOR INFORMATION


### Corresponding Author

**Wei-Lin Dai** − *Department of Chemistry and Shanghai Key Laboratory of Molecular Catalysis and Innovative Materials, Fudan University, Shanghai 200433, P.R. China;* orcid.org/0000-0003-4838-5678; Phone: +86 3124 9122; Email: wldai@fudan.edu.cn; Fax: +86 3124 2978

### Authors

**Quan Zhang** − *Department of Chemistry and Shanghai Key Laboratory of Molecular Catalysis and Innovative Materials, Fudan University, Shanghai 200433, P.R. China*

**Juhua Zhang** − *Department of Chemistry and Shanghai Key Laboratory of Molecular Catalysis and Innovative Materials, Fudan University, Shanghai 200433, P.R. China*

**Xiaohao Wang** − *Department of Chemistry and Shanghai Key Laboratory of Molecular Catalysis and Innovative Materials, Fudan University, Shanghai 200433, P.R. China*

**Lingfeng Li** − *Department of Chemistry and Shanghai Key Laboratory of Molecular Catalysis and Innovative Materials, Fudan University, Shanghai 200433, P.R. China*

**Ye-Fei Li** − *Department of Chemistry and Shanghai Key Laboratory of Molecular Catalysis and Innovative Materials, Fudan University, Shanghai 200433, P.R. China;* orcid.org/0000-0003-4433-7433

Complete contact information is available at: https://pubs.acs.org/10.1021/acscatal.0c05520


### Notes

The authors declare no competing financial interest.

## ■ ACKNOWLEDGMENTS

This work was financially supported by Natural Science Foundation of Shanghai (19ZR1403500), National Natural Science Foundation of China (NNSFC, No. 21373054), and Natural Science Foundation of Shanghai Science and Technology Committee (19DZ2270100). The authors would like to thank Dr. Songhai Xie (Dept. Chem., Fudan Univ.) for providing the convenience in the HRTEM measurements. The authors thank the referees for valuable suggestions regarding EXAFS and DFT calculations' analysis to help us in improving the quality of this work.

## ■ REFERENCES


(1) Pye, S.; Bradley, S.; Hughes, N.; Price, J.; Welsby, D.; Ekins, P. An Equitable Redistribution of Unburnable Carbon. *Nat. Commun.* **2020**, *11*, 3968.

(2) Chen, J.; Xie, Q.; Shahbaz, M.; Song, M.; Wu, Y. The Fossil Energy Trade Relations Among BRICS Countries. *Energy* **2021**, *217*, 119383.

(3) Shahsavari, A.; Akbari, M. Potential of Solar Energy in Developing Countries for Reducing Energy-Related Emissions. *Renewable Sustainable Energy Rev.* **2018**, *90*, 275−291.

(4) Tao, P.; Ni, G.; Song, C.; Shang, W.; Wu, J.; Zhu, J.; Chen, G.; Deng, T. Solar-Driven Interfacial Evaporation. *Nat. Energy* **2018**, *3*, 1031−1041.

(5) Kumar, A.; Kumar, A.; Krishnan, V. Perovskite Oxide Based Materials for Energy and Environment-Oriented Photocatalysis. *ACS Catal.* **2020**, *10*, 10253−10315.

(6) Peter, S. Reduction of $CO_2$ to Chemicals and Fuels: A Solution to Global Warming and Energy Crisis. *ACS Energy Lett.* **2018**, *3*, 1557−1561.

(7) Zhao, X.; Feng, J.; Liu, J.; Shi, W.; Yang, G.; Wang, G.; Cheng, P. An Efficient, Visible-Light-Driven, Hydrogen Evolution Catalyst NiS/$Zn_xCd_{1-x}S$ Nanocrystal Derived from A Metal-Organic Framework. *Angew. Chem., Int. Ed.* **2018**, *57*, 9790−9794.

(8) Zhang, M.; Hu, Q.; Ma, K.; Ding, Y.; Li, C. Pyroelectric Effect in CdS Nanorods Decorated with A Molecular Co-Catalyst for Hydrogen Evolution. *Nano Energy* **2020**, *73*, 104810.

(9) Wang, Z.; Li, C.; Domen, K. Recent Developments in Heterogeneous Photocatalysts for Solar-Driven Overall Water Splitting. *Chem. Soc. Rev.* **2019**, *48*, 2109−2125.

(10) Chen, X.; Xiao, S.; Wang, H.; Wang, W.; Cai, Y.; Li, G.; Qiao, M.; Zhu, J.; Li, H.; Zhang, D.; Lu, Y. MOFs Conferred with Transient Metal Centers for Enhanced Photocatalytic Activity. *Angew. Chem., Int. Ed.* **2020**, *59*, 17182−17186.

(11) Sun, L.; Zhuang, Y.; Yuan, Y.; Zhan, W.; Wang, X.; Han, X.; Zhao, Y. Nitrogen-Doped Carbon-Coated CuO-$In_2O_3$ p-n Heterojunction for Remarkable Photocatalytic Hydrogen Evolution. *Adv. Energy Mater.* **2019**, *9*, 1902839.

(12) Dai, B.; Fang, J.; Yu, Y.; Sun, M.; Huang, H.; Lu, C.; Kou, J.; Zhao, Y.; Xu, X. Construction of Infrared-Light-Responsive Photoinduced Carriers Driver for Enhanced Photocatalytic Hydrogen Evolution. *Adv. Mater.* **2020**, *32*, 1906361.

(13) Feng, X.; Pi, Y.; Song, Y.; Brzezinski, C.; Xu, Z.; Li, Z.; Lin, W. Metal-Organic Frameworks Significantly Enhance Photocatalytic Hydrogen Evolution and $CO_2$ Reduction with Earth-Abundant Copper Photosensitizers. *J. Am. Chem. Soc.* **2020**, *142*, 690−695.

(14) Gottschling, K.; Savasci, G.; Vignolo-Gonzalez, H.; Schmidt, S.; Mauker, P.; Banerjee, T.; Rovo, P.; Ochsenfeld, C.; Lotsch, B. V. Rational Design of Covalent Cobaloxime-Covalent Organic Framework Hybrids for Enhanced Photocatalytic Hydrogen Evolution. *J. Am. Chem. Soc.* **2020**, *142*, 12146−12156.
(15) Wang, L.; Xiao, H.; Cheng, T.; Li, Y.; Goddard, W. A. Pb-Activated Amine-Assisted Photocatalytic Hydrogen Evolution Reaction on Organic-Inorganic Perovskites. *J. Am. Chem. Soc.* **2018**, *140*, 1994−1997.
(16) Woods, D. J.; Hillman, S. A. J.; Pearce, D.; Wilbraham, L.; Flagg, L. Q.; Duffy, W.; McCulloch, I.; Durrant, J. R.; Guilbert, A. A. Y.; Zwijnenburg, M. A.; Sprick, R. S.; Nelson, J.; Cooper, A. I. Side-Chain Tuning in Conjugated Polymer Photocatalysts for Improved Hydrogen Production from Water. *Energy Environ. Sci.* **2020**, *13*, 1843−1855.
(17) Cheng, Z.; Wang, F.; Shifa, T.; Jiang, C.; Liu, Q.; He, J. Efficient Photocatalytic Hydrogen Evolution via Band Alignment Tailoring: Controllable Transition from Type-I to Type-II. *Small* **2017**, *13*, 1702163.
(18) Zhu, Y.; Marianov, A.; Xu, H.; Lang, C.; Jiang, Y. Bimetallic Ag-Cu Supported on Graphitic Carbon Nitride Nanotubes for Improved Visible-Light Photocatalytic Hydrogen Production. *ACS Appl. Mater. Interfaces* **2018**, *10*, 9468−9477.
(19) Wang, S.; Guan, B.; Wang, X.; Lou, X. Formation of Hierarchical $Co_9S_8$@$ZnIn_2S_4$ Heterostructured Cages as An Efficient Photocatalyst for Hydrogen Evolution. *J. Am. Chem. Soc.* **2018**, *140*, 15145−15148.
(20) Li, J.; Zhao, Y.; Xia, M.; An, H.; Bai, H.; Wei, J.; Yang, B.; Yang, G. Highly Efficient Charge Transfer at 2D/2D Layered P-$La_2Ti_2O_7$/$Bi_2WO_6$ Contact Heterojunctions for Upgraded Visible-Light-Driven Photocatalysis. *Appl. Catal., B* **2020**, *261*, 118244.
(21) Su, D.; Ran, J.; Zhuang, Z.; Chen, C.; Qiao, S.; Li, Y.; Wang, G. Atomically Dispersed Ni in Cadmium-Zinc Sulfide Quantum Dots for High-Performance Visible-Light Photocatalytic Hydrogen Production. *Sci. Adv.* **2020**, *6*, No. eaaz8447.
(22) Zhou, P.; Lv, F.; Li, N.; Zhang, Y.; Mu, Z.; Tang, Y.; Lai, J.; Chao, Y.; Luo, M.; Lin, F.; Zhou, J.; Su, D.; Guo, S. Strengthening Reactive Metal-support Interaction to Stabilize High-density Pt Single Atoms on Electron-deficient g-$C_3N_4$ for Boosting Photocatalytic $H_2$ Production. *Nano Energy* **2019**, *56*, 127−137.
(23) Chen, S.; Huang, D.; Xu, P.; Gong, X.; Xue, W.; Lei, L.; Deng, R.; Li, J.; Li, Z. Facet-Engineered Surface and Interface Design of Monoclinic Scheelite Bismuth Vanadate for Enhanced Photocatalytic Performance. *ACS Catal.* **2020**, *10*, 1024−1059.
(24) Zhu, Y.; Lv, C.; Yin, Z.; Ren, J.; Yang, X.; Dong, C.-L.; Liu, H.; Cai, R.; Huang, Y.-C.; Theis, W.; Shen, S.; Yang, D. A [001]-Oriented Hittorf's Phosphorus Nanorods/Polymeric Carbon Nitride Heterostructure for Boosting Wide-Spectrum-Responsive Photocatalytic Hydrogen Evolution from Pure Water. *Angew. Chem., Int. Ed.* **2020**, *59*, 868−873.
(25) Wang, S.; Guan, B.; Lu, Y.; Lou, X. Formation of Hierarchical $In_2S_3$-$CdIn_2S_4$ Heterostructured Nanotubes for Efficient and Stable Visible Light $CO_2$ Reduction. *J. Am. Chem. Soc.* **2017**, *139*, 17305−17308.
(26) Wang, S.; Wang, Y.; Zang, S.-Q.; Lou, X. Hierarchical Hollow Heterostructures for Photocatalytic $CO_2$ Reduction and Water Splitting. *Small Methods* **2020**, *4*, 1900586.
(27) Afroz, K.; Moniruddin, M.; Bakranov, N.; Kudaibergenov, S.; Nuraje, N. A Heterojunction Strategy to Improve the Visible Light Sensitive Water Splitting Performance of Photocatalytic Materials. *J. Mater. Chem. A* **2018**, *6*, 21696−21718.
(28) Mu, L.; Zhao, Y.; Li, A.; Wang, S.; Wang, Z.; Yang, J.; Wang, Y.; Liu, T.; Chen, R.; Zhu, J.; Fan, F.; Li, R.; Li, C. Enhancing Charge Separation on High Symmetry $SrTiO_3$ Exposed with Anisotropic Facets for Photocatalytic Water Splitting. *Energy Environ. Sci.* **2016**, *9*, 2463−2469.
(29) Wang, S.; Guan, B.; Lou, X. Construction of $ZnIn_2S_4$-$In_2O_3$ Hierarchical Tubular Heterostructures for Efficient $CO_2$ Photoreduction. *J. Am. Chem. Soc.* **2018**, *140*, 5037−5040.
(30) Sun, N.; Guan, Z.; Liu, Y.; Cao, Y.; Zhu, Q.; Liu, H.; Wang, Z.; Zhang, P.; Xu, B. Extended "Adsorption-Insertion" Model: A New Insight into the Sodium Storage Mechanism of Hard Carbons. *Adv. Energy Mater.* **2019**, *9*, 1901351.
(31) Zhang, G.; Chen, D.; Li, N.; Xu, Q.; Li, H.; He, J.; Lu, J. Construction of Hierarchical Hollow $Co_9S_8$/$ZnIn_2S_4$ Tubular Heterostructures for Highly Efficient Solar Energy Conversion and Environmental Remediation. *Angew. Chem., Int. Ed.* **2020**, *59*, 8255−8261.
(32) Zuo, G.; Wang, Y.; Teo, W. L.; Xie, A.; Guo, Y.; Dai, Y.; Zhou, W.; Jana, D.; Xian, Q.; Dong, W.; Zhao, Y. Ultrathin $ZnIn_2S_4$ Nanosheets Anchored on $Ti_3C_2T_X$ MXene for Photocatalytic $H_2$ Evolution. *Angew. Chem., Int. Ed.* **2020**, *59*, 11287−11292.
(33) Xu, J.; Qi, Y.; Wang, L. In Situ Derived $Ni_2P$/Ni Encapsulated in Carbon/g-$C_3N_4$ Hybrids from Metal-Organic Frameworks/g-$C_3N_4$ for Efficient Photocatalytic Hydrogen Evolution. *Appl. Catal., B* **2019**, *246*, 72−81.
(34) Yang, F.; Zhang, Q.; Zhang, L.; Cao, M.; Liu, Q.; Dai, W.-L. Facile Synthesis of Highly Efficient Pt/N-rGO/N-$NaNbO_3$ Nanorods toward Photocatalytic Hydrogen Production. *Appl. Catal., B* **2019**, *257*, 117901.
(35) Ye, K.; Li, Y.; Yang, H.; Li, M.; Huang, Y.; Zhang, S.; Ji, H. An Ultrathin Carbon Layer Activated $CeO_2$ Heterojunction Nanorods for Photocatalytic Degradation of Organic Pollutants. *Appl. Catal., B* **2019**, *259*, 118085.
(36) Sun, L.; Li, R.; Zhan, W.; Yuan, Y.; Wang, X.; Han, X.; Zhao, Y. Double-shelled Hollow Rods Assembled from Nitrogen/sulfur-codoped Carbon Coated Indium Oxide Nanoparticles as Excellent Photocatalysts. *Nat. Commun.* **2019**, *10*, 2270.
(37) Li, Y.; Wang, S.; Wang, P.; He, Y.; Wang, X.; Chang, K.; Lin, H.; Ding, X.; Chen, H.; Zhang, H.; Izumi, Y.; Kako, T.; Ye, J. Targeted Removal of Interfacial Adventitious Carbon Towards Directional Charge Delivery to Isolated Metal Sites for Efficient Photocatalytic $H_2$ Production. *Nano Energy* **2020**, *76*, 105077.
(38) Wang, S.; Wang, Y.; Zhang, S.; Zang, S.-Q.; Lou, X. Supporting Ultrathin $ZnIn_2S_4$ Nanosheets on Co/N-Doped Graphitic Carbon Nanocages for Efficient Photocatalytic $H_2$ Generation. *Adv. Mater.* **2019**, *31*, 1903404.
(39) Sun, L.; Zhuang, Y.; Yuan, Y.; Zhan, W.; Wang, X.; Han, X.; Zhao, Y. Nitrogen-Doped Carbon-Coated CuO-$In_2O_3$ p-n Heterojunction for Remarkable Photocatalytic Hydrogen Evolution. *Adv. Energy Mater.* **2019**, *9*, 1902839.
(40) Menon, S.; Hafeez, H.; Gupta, B.; Baskar, K.; Bhalerao, G.; Hussain, S.; Neppolian, B.; Singh, S. ZnO:InN Oxynitride: A Novel and Unconventional Photocatalyst for Efficient UV-visible Light Driven Hydrogen Evolution from Water. *Renewable Energy* **2019**, *141*, 760−769.
(41) Ning, Q.; Wu, G.; Wang, Y.; Sun, Y.; Feng, W. Synthesis of a Novel $In_2O_3$-InN Bottle Nanotube Using In-Situ Partial Oxidation with Enhanced Gas Sensing Platform to Detect $NO_2$. *Crystals* **2020**, *10*, 570.
(42) Ma, D.; Shi, J.-W.; Zou, Y.; Fan, Z.; Shi, J.; Cheng, L.; Sun, D.; Wang, Z.; Niu, C. Multiple Carrier-Transfer Pathways in Flower-Like $In_2S_3$/$CdIn_2S_4$/$In_2O_3$ Ternary Heterostructure for Enhanced Photocatalytic Hydrogen Production. *Nanoscale* **2018**, *10*, 7860−7870.
(43) Li, R.; Sun, L.; Zhan, W.; Li, Y.-A.; Wang, X.; Han, X. Engineering an Effective Noble-Metal-Free Photocatalyst for Hydrogen Evolution: Hollow Hexagonal Porous Micro-Rod Assembled by $In_2O_3$@Carbon Core-Shell Nanoparticles. *J. Mater. Chem. A* **2018**, *6*, 15747−15754.
(44) Chen, S.; Zhou, X.; Liao, J.; Yang, S.; Zhou, X.; Gao, Q.; Zhang, S.; Fang, Y.; Zhong, X.; Zhang, S. FeNi Intermetallic Compound Nanoparticles Wrapped with N-doped Graphitized Carbon: A Novel Cocatalyst for Boosting Photocatalytic Hydrogen Evolution. *J. Mater. Chem. A* **2020**, *8*, 3481−3490.
(45) Zhan, W.; Yuan, Y.; Sun, L.; Yuan, Y.; Han, X.; Zhao, Y. Hierarchical NiO@N-Doped Carbon Microspheres with Ultrathin Nanosheet Subunits as Excellent Photocatalysts for Hydrogen Evolution. *Small* **2019**, *15*, 1901024.
(46) Wang, J.; Chen, Y.; Zhou, W.; Tian, G.; Xiao, Y.; Fu, H.; Fu, H. Cubic Quantum Dot/Hexagonal Microsphere $ZnIn_2S_4$ Heterophase Junctions for Exceptional Visible-Light-Driven Photocatalytic $H_2$ Evolution. *J. Mater. Chem. A* **2017**, *5*, 8451−8460.


https://doi.org/10.1021/acscatal.0c05520
ACS Catal. 2021, 11, 6276−6289

(47) Meng, X.; Zhang, C.; Dong, C.; Sun, W.; Ji, D.; Ding, Y. Carbon Quantum Dots Assisted Strategy to Synthesize Co@NC for Boosting Photocatalytic Hydrogen Evolution Performance of CdS. *Chem. Eng. J.* **2020**, *389*, 124432.
(48) Cao, S.; Piao, L. Considerations for a More Accurate Evaluation Method for Photocatalytic Water Splitting. *Angew. Chem., Int. Ed.* **2020**, *59*, 18312−18320.
(49) Melchionna, M.; Fornasiero, P. Updates on the Roadmap for Photocatalysis. *ACS Catal.* **2020**, *10*, 5493−5501.
(50) Bettucci, O.; Skaltsas, T.; Calamante, M.; Dessì, A.; Bartolini, M.; Sinicropi, A.; Filippi, J.; Reginato, G.; Mordini, A.; Fornasiero, P.; Zani, L. Combining Dithienosilole-Based Organic Dyes with a Brookite/Platinum Photocatalyst toward Enhanced Visible-Light-Driven Hydrogen Production. *ACS Appl. Energy Mater.* **2019**, *2*, 5600−5612.
(51) Bartolini, M.; Gombac, V.; Sinicropi, A.; Reginato, G.; Dessì, A.; Mordini, A.; Filippi, J.; Montini, T.; Calamante, M.; Fornasiero, P.; Zani, L. Tuning the Properties of Benzothiadiazole Dyes for Efficient Visible Light-Driven Photocatalytic $H_2$ Production under Different Conditions. *ACS Appl. Energy Mater.* **2020**, *3*, 8912−8928.
(52) Li, H.; Wells, N.; Chong, B.; Xu, B.; Wei, J.; Yang, B.; Yang, G. The Layered Cadmium Phosphorus Trichalcogenides Nanosheet with Anion Mono-Doping: A New Candidate for Solar-Driven Water Splitting. *Chem. Eng. Sci.* **2021**, *229*, 116069.
(53) Gunasekar, G.; Shin, J.; Jung, K.-D.; Park, K.; Yoon, S. Design Strategy toward Recyclable and Highly Efficient Heterogeneous Catalysts for the Hydrogenation of $CO_2$ to Formate. *ACS Catal.* **2018**, *8*, 4346−4353.
(54) Ma, B.; Li, X.; Li, D.; Lin, K. A Difunctional Photocataly tic $H_2$ Evolution Composite Co-catalyst Tailored by Integration with Earth-Abundant Material and Ultralow Amount of Noble Metal. *Appl. Catal., B* **2019**, *256*, 117865.
(55) Wang, B.; Guo, S.; Xin, X.; Zhang, Y.; Wang, Y.; Li, C.; Song, Y.; Deng, D.; Li, X.; Sobrido, A. J.; Titirici, M.-M. Heat Diffusion-Induced Gradient Energy Level in Multishell Bisulfides for Highly Efficient Photocatalytic Hydrogen Production. *Adv. Energy Mater.* **2020**, *10*, 2001575.
(56) Zhang, S.; Cheng, G.; Guo, L.; Wang, N.; Tan, B.; Jin, S. Strong-Base-Assisted Synthesis of A Crystalline Covalent Triazine Framework with High Hydrophilicity via Benzylamine Monomer for Photocatalytic Water Splitting. *Angew. Chem., Int. Ed.* **2020**, *59*, 6007−6014.
(57) Lin, B.; Yang, G.; Wang, L. Stacking-Layer-Number Dependence of Water Adsorption in 3D Ordered Close-Packed g-$C_3N_4$ Nanosphere Arrays for Photocatalytic Hydrogen Evolution. *Angew. Chem., Int. Ed.* **2019**, *58*, 4587−4591.
(58) Yuan, Y.-J.; Chen, D.; Zhong, J.; Yang, L.-X.; Wang, J.; Liu, M.-J.; Tu, W.-G.; Yu, Z.-T.; Zou, Z.-G. Interface Engineering of A Noble-Metal-Free 2D-2D $MoS_2$/Cu-$ZnIn_2S_4$ Photocatalyst for Enhanced Photocatalytic $H_2$ Production. *J. Mater. Chem. A* **2017**, *5*, 15771−15779.
(59) Yuan, W.; Cheng, L.; An, Y.; Lv, S.; Wu, H.; Fan, X.; Zhang, Y.; Guo, X.; Tang, J. Laminated Hybrid Junction of Sulfur-Doped $TiO_2$ and A Carbon Substrate Derived from $Ti_3C_2$ MXenes: toward Highly Visible Light-Driven Photocatalytic Hydrogen Evolution. *Adv. Sci.* **2018**, *5*, 1700870.
(60) Zhao, Q.; Sun, J.; Li, S.; Huang, C.; Yao, W.; Chen, W.; Zeng, T.; Wu, Q.; Xu, Q. Single Nickel Atoms Anchored on Nitrogen-Doped Graphene as A Highly Active Cocatalyst for Photocatalytic $H_2$ Evolution. *ACS Catal.* **2018**, *8*, 11863−11874.
(61) Li, L.; Li, Y.; Liu, Z. $CO_2$ Photoreduction via Quantum Tunneling: Thin $TiO_2$-Coated GaP with Coherent Interface to Achieve Electron Tunneling. *ACS Catal.* **2019**, *9*, 5668−5678.
(62) Qi, J.; Świątowska, J.; Skeldon, P.; Marcus, P. Chromium Valence Change in Trivalent Chromium Conversion Coatings on Aluminium Deposited Under Applied Potentials. *Corros. Sci.* **2020**, *167*, 108482.
(63) Cho, J.; Suwandaratne, N. S.; Razek, S.; Choi, Y.-H.; Piper, L. F. J.; Watson, D. F.; Banerjee, S. Elucidating the Mechanistic Origins of Photocatalytic Hydrogen Evolution Mediated by $MoS_2$/CdS Quantum-Dot Heterostructures. *ACS Appl. Mater. Interfaces* **2020**, *12*, 43728−43740.
(64) Jin, P.; Wang, L.; Ma, X.; Lian, R.; Huang, J.; She, H.; Zhang, M.; Wang, Q. Construction of Hierarchical $ZnIn_2S_4$@PCN-224 Heterojunction for Boosting Photocatalytic Performance in Hydrogen Production and Degradation of Tetracycline Hydrochloride. *Appl. Catal., B* **2021**, *284*, 119762.
(65) Yu, H.; Shi, R.; Zhao, Y.; Bian, T.; Zhao, Y.; Zhou, C.; Waterhouse, G. I. N.; Wu, L.-Z.; Tung, C.-H.; Zhang, T. Alkali-Assisted Synthesis of Nitrogen Deficient Graphitic Carbon Nitride with Tunable Band Structures for Efficient Visible-Light-Driven Hydrogen Evolution. *Adv. Mater.* **2017**, *29*, 1605148.


https://doi.org/10.1021/acscatal.0c05520
*ACS Catal.* 2021, 11, 6276−6289